Analysis of unsteady thermo-solutal MoS$_2$-EO Brinkman electro-conductive reactive nanofluid transport in a hybrid rotating Hall MHD generator

MD. Shamsuddin [a],[*], O. Anwar Bég [b], Nevzat Akkurt [c], Henry J. Leonard [b], Tasveer A. Bég [d]

[a] *Department of Mathematics, School of Sciences, SR University, Warangal 506371, Telangana, India*
[b] *Multi-Physical Engineering Sciences Group, Mechanical Engineering Department, Corrosion and Coatings Lab, Room 3-08, SEE Building, University of Salford, Manchester, M54WT, UK*
[c] *Department of Mechanical Engineering, Munzur University, Tunceli 62000, Turkey*
[d] *Engineering Mechanics Research, Israfil House, Dickenson Rd., Manchester, M13, UK*

ARTICLE INFO

ABSTRACT

MHD rotating generators offer a plausible renewable energy mechanism. New designs are emerging in which nanotechnology is contributing. Such systems are increasingly deploying more complex functional fluid materials such as base fluids containing magnetic nanoparticles which constitute electromagnetic nanofluids and can be tuned to enhance efficiencies. Motivated by these developments, a mathematical model is presented for the combined effects of Hall current, heat source, chemical reaction and radiative flux on the unsteady rotating thermo-solutal magnetohydrodynamic transport of a Molybdenum disulphide (MoS$_2$)-EO oil electroconductive Brinkman nanofluid to study the boundary layer characteristics in the vicinity of the side wall of an MHD generator system. The governing dimensional conservation equations are scaled using appropriate transformations into a system of dimensionless coupled partial differential equations. Under appropriate initial and boundary conditions, solutions are derived using the Laplace Transform Method (LTM) and complex variables. The physical impacts of the magnetic, nanoscale, thermal and species control parameters on primary and secondary velocity, temperature and concentration are visualized graphically. The judicious doping of the base fluid with MoS$_2$ nanoparticles is shown to achieve superior thermal performance for MHD rotating energy generators.

1. Introduction

In the 21st century the drive for renewable, sustainable energy systems has increased considerably. Although wind, wave and tidal systems have been extensively explored, these remain highly localized. An alternative system which is significantly more portable and deployable irrespective of geographical location is the magnetohydrodynamic energy generator. Original work on such systems which utilize a hot conducting medium (e.g. plasma stream) under applied magnetic field to directly produce electricity, was limited by the quality of working fluids and magnetic materials available. In recent years there has been a revitalization in MHD technology with the development of more efficient fluent media and operational control procedures. Many different configurations have emerged including Faraday generators, pulsed generators and liquid metal generators. In addition, MHD generator technology has been coupled with other renewable systems and power sources. These include solar MHD systems deploying electrolytic solutions,[1] oscillatory Faraday generators connected to continuous electrodes for grid deployment[2,3] and sea water-based

Hall generators.[4] The latter exploit the Hall current which is mobilized when the high Faraday electric current which flows across a duct reacts with the applied magnetic field. This generates the Hall current which is orientated perpendicular to the Faraday current and produces a secondary (cross) flow. Hall generators operate in a similar fashion to a mechanical dynamo, although in the former the motion of a metallic (solid) conductor in the magnetic field produces electrical current. In the Hall MHD generator, the conducting fluid replaces the metal solid conductor. A further modification of the MHD generators features *rotation* of the system about a specific axis. This generates a Coriolis force which can be manipulated to ramp up the flow rate and other characteristics. This methodology has been deployed in for example rotating alternating current disk generators[5] and other designs such as the segmented Faraday generator and the Hall generator,[6] to achieve higher power efficiencies. To simulate the dynamics of conducting fluids in MHD generators, the science of magnetohydrodynamics (MHD) must be combined with heat and mass transfer and other aspects.[7] Critical to performance, is the behavior at the electrode walls in these

---

systems. This features boundary layer phenomena which must be carefully controlled to avoid separation, flow reversal and interference with the duct core flow.[8] With thicker momentum boundary layers, the negative impact of discharge electrode on the flow is also reduced. The elimination of boundary-layer separation also enhances conducting fluid properties in the generator and boosts Hall parameter effects and electrical efficiency. A number of researchers have therefore examined in detail the near-wall characteristics of Hall MHD generator flows using both analytical and computational approaches and considering both laminar and turbulent situations. Bég et al.[9] computed the hydromagnetic boundary layer flow for a micropolar conducting fluid along a non-linear stretching/contracting wall under oblique magnetic field and with Hall current and Ohmic heating (Joule dissipation). They used a Nachtsheim–Swigert iteration technique with the fourth–fifth order Runge–Kutta integration method, homotopy and Adomain decomposition methods to solve the self-similar boundary layer problem. They noted that primary and secondary flows are enhanced with greater Hall parameter and non-isothermal wall index and that wall couple stress and Nusselt number are also ramped up. Pengyyu et al.[10] computed the supersonic non-equilibrium plasma boundary layer in an MHD generator system, identifying the significant interaction between the wall electrode and plasma and intensification of strong current eddies in the boundary layer with larger magnetic field strengths. Biswas et al.[11] computed the two-dimensional compressible turbulent boundary layer helium/argon flow characteristics on a 100 MW thermal input supersonic disk MHD generator wall. They observed that momentum boundary layer thickness is enhanced downstream in the channel for both argon and helium whereas for helium there is strong boundary layer separation with high enthalpy extraction conditions. They further identified that Hall current is strongly suppressed and reversed close to the insulator wall at the channel downstream section, whereas Faraday current is more gradually altered for both helium and argon. A number of investigators have also computed the effects of Hall current in rotating MHD generator plate boundary layer flows with heat and mass transfer. Hussain et al.[12] considered additionally heat generation and reactive species present in the streaming flow, and using a Laplace transform method (LTM) showed that increased rotation suppresses the primary flow whereas greater Hall current enhances the secondary flow in the boundary layer and stronger chemical reaction boosts the primary skin friction. Seth et al.[13] studied the influence of impulsive wall motion and ramped wall temperature on rotating Hall current near wall flows with natural convective heat and mass transfer. They showed that Hall current accelerates secondary fluid velocity throughout the boundary layer region, but only boosts the primary fluid velocity in the region near the plate. They also found that for both ramped temperature and isothermal cases, the Hall current, thermal buoyancy force, concentration buoyancy force and mass diffusion suppress primary skin friction but increase secondary skin friction. Bég et al.[14] employed an electro-thermal network simulation code (PSPICE) to compute the viscous plasma flow with Hall current and inclined magnetic field in a rotating MHD energy generator duct containing a porous medium. They showed that primary and secondary flows are boosted with higher medium permeability and that increasing Hall current depletes the primary flow but enhances the secondary flow.

In engineering and science, manipulating properties of working fluids at the microscale and nanoscale has received increasing attention. In the 1990s the new area of *nanofluids* was introduced.[15] These colloidal suspensions were engineered by dispersing nano-meter-size structures (particles, fibers, tubes, droplets) in base fluids which was shown to enhance macroscale and mega-scale properties such as thermal conductivity via careful manipulation of nanoscale physics (structures, properties and activities). Conventional liquids used in engineering energy systems such as kerosene, polyethylene glycol, ethylene glycol, water, EO, etc., generally have low thermal conductivity, heat capacity etc. The addition of nanoparticles to these fluent media results in a strong increase in thermal conductivity, but

without agglomeration and clustering effects.[16] A further subset of nanofluids which has emerged are *functional magnetic nanofluids*.[17] These utilize the magnetic properties of specific nanoparticles to boost electro-conductivity (and other properties) of working base fluids and have significant potential in MHD energy systems as thermoelectric materials. Many superior properties such as high surface areas, tunable structures which respond to external magnetic fields have mobilized the introduction of magnetic nanofluids in many other areas also including environmental, biomedical, catalysis, drug delivery and bioimaging. The overall performance is strongly dependent on base solvents deployed under different reaction conditions. In renewable energy systems, magnetic nanofluids have been explored in AC MHD duct flows,[18] supercapacitors,[19,20] photo thermal convection in nano-solar collectors[21] (where they have boosted thermal efficiency to over 65%) and geothermal power production.[22,23] These applications have featured many different types of magnetic nanoparticles such as Cobalt and iron oxide in combination with diverse base fluids (ethylene glycol, water, kerosene etc.). An alternative nanomaterial is molybdenum disulphide (MoS_2), which has excellent magnetic, optical and thermal stability properties and has been implemented in a range of energy applications including piezoelectric energy harvesting,[24,25] more recently in ferromagnetic power systems,[26,27] solar radiation[28] and electromagnetohydrodynamic (EMHD) fluid flows.[29]

Mathematical models of magnetic nanofluid transport with Hall currents and boundary layer phenomena have also received some attention in recent years as these are relevant to the analysis of near wall characteristics of nano-enhanced MHD generator systems. Reddy et al.[30] used Keller's second order accurate finite difference scheme with Buongiorno's two component nanoscale model to compute the combined effect of Hall current and ion slip on dissipative electro-conductive nanofluid wall generator boundary layer flow with distensibility in the wall. They showed that increasing Hall and ion slip both enhance the primary flow whereas they suppress secondary flow, temperature and nanoparticle concentration magnitudes. They further observed that greater Brownian motion boosts both primary and secondary flow and temperature but reduces nanoparticle concentration. Increasing magnetic field was observed also to elevate secondary skin friction on the electrode wall but depleted primary skin friction. This study was confined to the linear MHD generator design. However, other articles have addressed Hall current rotating MHD generator flows deploying magnetic nanofluids. Wahid and Akl[31] used an optimal homotopy analysis method to compute the rotating disk MHD generator swirling flow for a radiative magnetic nanofluid with Hall effect. They observed that increasing Hall current decreases primary skin friction and also reduces the Nusselt number (heat transfer rate to the wall) and that magnetic Al_2O_3 nanoparticles produce higher Nusselt numbers than magnetized CuO nanoparticles. They further observed that increasing Hall current enhances the radial velocity component and temperature, whereas increasing Hartmann number induces the opposite effect. Further studies have been presented by Gumber et al.[32] (for non-Newtonian micropolar hybrid nanofluid with radiation and suction/injection), Ali et al.[33] (for magnetic hybrid nanofluids between Couette channel) and Takhar et al.[34] (rotating fluid with magnetic and Hall currents). All these investigations have confirmed the significant influence of magnetic nanoparticle properties and Hall current on transport characteristics in MHD generator configurations.

Several formulations exist for simulating nanoscale effects in viscous fluids. These include the Buongiorno model[30] which includes a species diffusion equation in addition to the energy conservation equation and emphasizes Brownian motion and thermophoretic body force effects. Another popular approach is the Tiwari–Das formulation[32] which allows different nanoparticle materials to be simulated but does not feature species diffusion (mass transfer). An alternative model is the *generalized Brinkman-type model*[35] which is a modification of the Hamilton–Crosser model, sphericity is the ratio of surface area of the sphere to the surface area of real particles with equal volumes. This model introduces a special drag force parameter termed
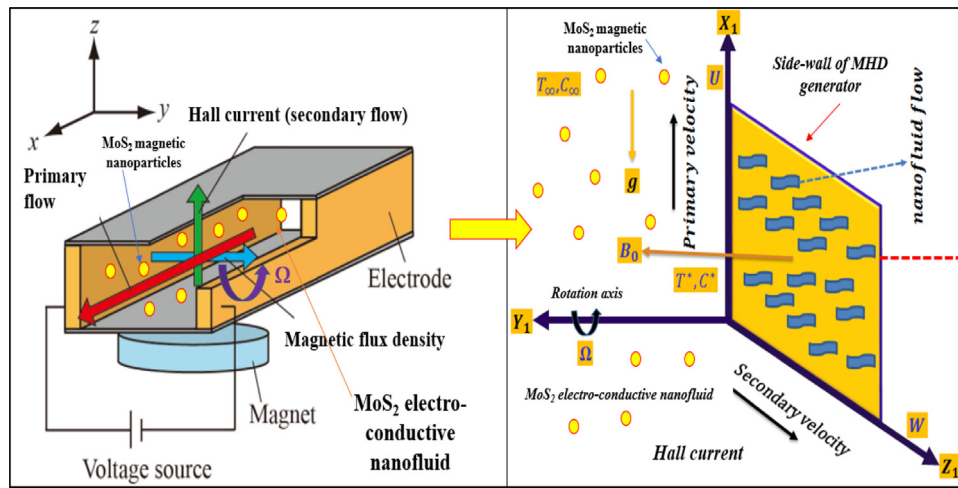
Fig. 1. Left — Hybrid rotating MHD Hall nanofluid generator; right — side wall boundary layer flow model.

the Brinkman parameter which can be used to analyze the relative effect of drag force on the nanoparticles to inertial force. It also allows for the inclusion of energy conservation and mass transfer and appropriate relationships are required for the viscosity, density, thermal conductivity and so on in terms of actual nanoparticle volume fraction. The generalized Brinkman model has been successfully deployed in a number of studies relevant to MHD energy generators. Jan et al.[36] have investigated the transport of a magnetic Molybdenum Disulphide (MoS$_2$)/oil- based general Brinkman-type nanofluid from an oscillating vertical surface to a porous medium with radiative flux. They used fractional Atangana–Baleanu derivatives and Laplace transforms to derive solutions for velocity and temperature and Nusselt number for a range of volume fractions. Further studies deploying Molybdenum Disulphide (MoS$_2$)/oil- based general Brinkman-type nanofluids include Ali et al.[37] (on rotating disk MHD generator flows with Hall currents) and Mishra and Upreti[38] (with Buongiorno model and nanoparticle effects for different water and ethylene glycol base fluids). Several other contributions on the different nanoparticles are covered in the studies.[39–42]

A scrutiny of the literature has revealed that, thus far, the *rotating thermo-solutal transport in magnetized Molybdenum Disulphide (MoS$_2$)/oil-based general Brinkman-type nanofluid with the simultaneous effects of chemical reaction, Hall current, radiative flux and heat generation* has not been addressed. This constitutes the novelty and focus of the present article. Chemical reactions are relevant to corrosion effects at the electrode walls in actual MHD generators.[43] High operational temperatures required for corrosion protection of aerospace gas turbine blades.[44] The mathematical model is formulated for the near-wall transport regime. The non-dimensional boundary layer equations for electroconductive nanofluid are rendered dimensionless via appropriate scaling similarity transformations. The dimensionless coupled partial differential equation boundary value problem is then solved with appropriate boundary conditions, analytically via a Laplace Transform Method (LTM) with complex variables. The physical impacts of the magnetic, nanoscale, thermal and species control parameters on primary and secondary (cross flow) velocity, temperature, concentration, primary and secondary skin friction (wall shear stress), Nusselt number and Sherwood number are visualized graphically, for physically realistic ranges of selected parameters. Detailed interpretation is provided with relevance to rotating Hall MHD generator flow characteristics and implications for efficiency performance. Future pathways for extending the analysis are also given.

2. Mathematical model

The focus here is the near-wall boundary layer transport characteristics on the side wall of a rotating hybrid nanofluid Hall MHD generator. We consider the unsteady flow of an incompressible electrically conducting viscous MoS$_2$ engine-oil based nanofluid with heat and mass transfer on the side wall of a rotating Hall generator under a transverse (vertical) magnetic field of strength $B0$. The Hall current is generated transverse to the applied magnetic field and significant thermal radiation flux is present due to high temperature. Heat source is also considered. A first order model is deployed for the reactive nanoparticle species. The entire system rotates in unison about the Y_1 axis. At $t = 0$ the magnetic nanofluid fluid is at rest with ambient temperature T_∞ and concentration C_∞. After $t = t_1$, the wall starts moving with a velocity of constant amplitude u_0. Wall temperature and wall concentration are elevated to T_w and C_w as illustrated in Fig. 1. Surface electrical polarization at the wall is ignored as are magnetic induction effects (small magnetic Reynolds number). Ohm's law in generalized form with Hall current may be stated as follows:

$$\vec{J} + \frac{\omega_e \tau_e}{B_0}\left(\vec{J} \times \vec{B}\right) = \sigma\left[\vec{E} + \vec{U} \times \vec{B} + \frac{1}{e\,\eta_e}\nabla p_e\right] \tag{2.1}$$

Here $\vec{J} = (J_x, J_y, J_z)$ is the electrical current density, $\vec{B} = (0, B_o, 0)$ is magnetic field vector, $\vec{E} = (0, E_o, 0)$ is electrical field vector, $\vec{U} = (U, V, W)$ is velocity vector, ω_i and τ_i are cyclotron frequency and collision time for electrons, σ is electrical conductivity of the fluid, e is electronic charge, η_e is number density of electrons, ∇p_e is pressure exerted on an electron. For weakly ionized fluids, $J_y = 0$. It emerges that electrical field $E = 0$. Then the electrical current density components with Hall effect (m) assume the following form[45,46]:

$$\left.\begin{aligned} J_x &= \frac{\sigma B_o}{\left(1 + m^2\right)}(U + mW) \\ J_z &= \frac{\sigma B_o}{\left(1 + m^2\right)}(mU - W) \end{aligned}\right\} \tag{2.2}$$

Here the Hall parameter is defined as:

$$m = \omega_e \tau_e \tag{2.3}$$

In practical rotating MHD generators, $\omega_e \tau_e \sim O(1)$.[47] The retained velocity components in (2.2) are the U and W i.e. primary and secondary velocity.

The governing conservation partial differential equations for the magnetohydrodynamic thermo-solutal convection (momentum, heat and mass transfer) in a Brinkman MoS$_2$ engine-oil based nanofluid transport along a side wall, rotating at constant angular velocity, Ω, in the presence of chemical reaction, thermal radiation, heat generation and Hall current under the Boussinesq approximation, are obtained by extending the model in Ref. 37 (with chemical reaction and heat

Table 1
Engine oil and MoS$_2$ thermophysical properties – from Jan et al.[36]

	c_p (JK/kg)	$\beta \times 10^{-5}$ (1/K)	ρ (kg/m)	k (W/mK)	σ (S m^{-1})
EO	2048	0.00007	863	0.1404	2.09×10^{-4}
MoS$_2$	397.21	2.8424	5.06×10^3	904.4	55×10^{-6}

generation and mass transfer). These boundary layer equations take the form:

$$U_{t_1} + \beta U - 2\Omega W = \frac{\mu_{nf}}{\rho_{nf}} U_{Y_1 Y_1} - \frac{\sigma_{nf} B_0^2}{\rho_{nf}(1+m^2)}(U + mW)$$
$$\left. \begin{array}{r} +g\beta_{nf}^*(C^* - C_\infty) + \\ g\beta_{nf}(T^* - T_\infty) \end{array} \right\} \qquad (2.4)$$

$$W_{t_1} + \beta W + 2\Omega U = \frac{\mu_{nf}}{\rho_{nf}} W_{Y_1 Y_1} + \frac{\sigma_{nf} B_0^2}{\rho_{nf}(1+m^2)}(mU - W) \qquad (2.5)$$

$$(\rho c_p)_{nf} T_{t_1}^* = k_{nf} T_{Y_1 Y_1}^* - q_{rY_1} + Q_0(T^* - T_\infty) \qquad (2.6)$$

$$C_{t_1}^* = D C_{Y_1 Y_1}^* - K_1(C^* - C_\infty) \qquad (2.7)$$

Here U_{t_1} is a time derivative of primary velocity, W_{t_1} is a time derivative of secondary velocity, β is Brinkman (drag force/inertial force) nanoparticle parameter, μ_{nf} is the Brinkman nanofluid dynamic viscosity, ρ_{nf} is density of nanofluid, σ_{nf} is electrical conductivity of nanofluid, g is gravity, β_{nf}^* is the volumetric thermal expansion coefficient, β_{nf} is volumetric solutal expansion coefficient, T^* is temperature of nanofluid, C^* is the concentration of reactive species, k_{nf} is thermal conductivity of nanofluid, q_{rY_1} is radiative flux in the Y_1 direction, Q_0 is heat generation coefficient, D is molecular diffusivity of the reactive species and K_1 is the chemical reaction rate. The working magnetic Brinkman nanofluid is assumed to be optically thick and absorbing and emitting but not scattering for which the Rosseland diffusion flux model is appropriate. The following initial and boundary conditions are imposed[34]:

$$\left. \begin{array}{r} U(Y_1, 0) = 0, W(Y_1, 0) = 0, T^*(Y_1, 0) = T_\infty, C^*(Y_1, 0) = C_\infty, \\ U(0, t_1) = \Delta t, \quad W(0, t_1) = 0, T^*(0, t_1) = T_\infty + (T_w - T_\infty) At_1, \\ C^*(0, t_1) = C_\infty + (C_w - C_\infty) At_1, \\ U(\infty, t_1) = 0, W(\infty, t_1) = 0, T^*(\infty, t_1) = T_\infty, C^*(\infty, t_1) = C_\infty. \end{array} \right\} \qquad (2.8)$$

For generalized Brinkman nanofluids, the appropriate expressions for thermophysical properties, $\frac{\sigma_{nf}}{\sigma_f}, (\rho c_p)_{nf}, \mu_{nf}, (\rho\beta)_{nf}, \frac{k_{nf}}{k_f}$ and $(\rho\beta^*)_{nf}$, following,[34] may be stated as:

$$\left. \begin{array}{r} \frac{\sigma_{nf}}{\sigma_f} = \left[\frac{3\varphi(\sigma-1)}{(2+\sigma) - \varphi(\sigma-1)} + 1 \right], (\rho c_p)_{nf} = (\rho c_p)_s \varphi - (\rho c_p)_f (\varphi-1), \\ \mu_{nf} = \frac{\mu_f}{(1-\varphi)^{2.5}}, (\rho\beta)_{nf} = (\rho\beta)_s \varphi - (\rho\beta)_f (\varphi-1), \\ (\rho)_{nf} = (\rho)_s \varphi - (\rho)_f (\varphi-1), (\rho\beta^*)_{nf} = (\rho\beta^*)_s \varphi + (\rho\beta^*)_f (1-\varphi), \\ \frac{k_{nf}}{k_f} = \left[\frac{2k_f + k_s - 2\varphi(k_f - k_s)}{2k_f + k_s - \varphi(k_f - k_s)} \right], \sigma = \frac{\sigma_s}{\sigma_f} \end{array} \right\} \qquad (2.9)$$

Oztop and Abu Nada[48] showed that the above expressions are suitable for nanoparticles of spherical shape, as considered in the present study. Engine-oil base fluid and thermophysical properties of spherical MoS$_2$ nanoparticles are extracted from Ref. 36 and given in Table 1.

We consider the Rosseland diffusion flux approximation for radiative heat transfer, in which $q_{rY_1} = -\frac{4\sigma^*}{3k^*} T_{Y_1}^{*4}$ wherein σ^* is the Stefan–Boltzmann constant and k^* is the mean radiation absorption constant. Considering extremely small differences between the nanofluid bulk

temperature, T^* and the free stream temperature (at the edge of the boundary layer), T_∞, via a Taylor series expansion, neglecting second and higher order terms, it follows that $T^{*4} + 3T_\infty^3 = 4T_\infty^3 T^*$. Implementing this in the radiative flux term in Eq. (6), the following energy (thermal boundary layer) equation is obtained:

$$(\rho c_p)_{nf} T_{t_1}^* = \left(k_{nf} + \frac{16 T_\infty^3}{3k^*} \right) T_{Y_1 Y_1}^* + Q_0(T^* - T_\infty) \qquad (2.10)$$

To solve the primitive form of the conservation equations (2.4), (2.5), (2.7), (2.10) under conditions (2.8) is challenging to solve even numerically and intractable analytically. A set of non-dimensional variables are therefore invoked to transform the boundary value problem into a form amenable for analytical (closed form) solutions. Defining:

$$\left. \begin{array}{r} U = \bar{u} u_0, \quad Y = \frac{V y}{u_0}, \quad t_1 = \frac{V t}{u_0^2}, \quad W = \bar{w} u_0, \\ \bar{\theta}(T_w - T_\infty) = T^* - T_\infty, \bar{C}(C_w - C_\infty) = C^* - C_\infty \end{array} \right\} \qquad (2.11)$$

Inserting the above non-dimensional variables in Eqs. (2.4)–(2.10) we obtain the non-dimensional equations:

$$\bar{u}_t + \delta\bar{u} - 2\xi\bar{w} = \frac{1}{Re}\bar{u}_{yy} - \frac{M^*}{1+m^2}(\bar{u} + m\bar{w}) + Gr^*\bar{\theta} + Gm^*\bar{C} \qquad (2.12)$$

$$\bar{w}_t + \delta\bar{w} + 2\xi\bar{u} = \frac{1}{Re}\bar{w}_{yy} + \frac{M^*}{1+m^2}(m\bar{u} - \bar{w}) \qquad (2.13)$$

$$\bar{\theta}_t = \frac{1}{Pr_{eff}}\bar{\theta}_{yy} + \lambda^* Q\bar{\theta} \qquad (2.14)$$

$$Sc\bar{C}_t = \bar{C}_{yy} - Sc\ K_{ch}\ \bar{C} \qquad (2.15)$$

The dimensionless initial and boundary conditions are:

$$\left. \begin{array}{r} \bar{u}(y, 0) = 0, \ \bar{w}(y, 0) = 0, \ \bar{\theta}(y, 0) = 0, \ \bar{C}(y, 0) = 0, \\ \bar{u}(0, t) = \xi t, \ \bar{w}(0, t) = 0, \ \bar{\theta}(0, t) = t, \ \bar{C}(0, t) = t, \\ \bar{u}(\infty, t) = 0, \ \bar{w}(\infty, t) = 0, \ \bar{\theta}(\infty, t) = 0, \ \bar{C}(\infty, t) = 0 \end{array} \right\} \qquad (2.16)$$

Here the following notation applies:

$$\left. \begin{array}{r} Re = (1-\varphi)^{2.5}\left[(1-\varphi) + \varphi\frac{\rho_s}{\rho_f} \right], \xi = \frac{\Omega\nu}{u_0^2}, \varphi_1 = \left\{ 1 + \frac{3\varphi(\sigma-1)}{(\sigma+2) - \varphi(\sigma-1)} \right\}, \\ M = \frac{\sigma_f \nu B_0^2}{u_0^2 \rho_f}, \delta = \frac{\beta\nu}{u_0^2}, \varphi_2 = \frac{\varphi\rho_s\left(\frac{\beta_s}{\beta_f}\right) - (\varphi-1)\rho_f}{(1-\varphi)\rho_f + \varphi\rho_s}, M^* = \frac{\varphi_1 M}{(1-\varphi)^{-2.5} Re}, \\ Gr^* = Gr\varphi_2, \ Gr = \frac{(T_w - T_\infty) g\nu\beta_f}{u_0^3}, Gm^* = Gm\varphi_3, Gm = \frac{(C_w - C_\infty) g\nu\beta_f^*}{u_0^3}, \\ \varphi_3 = \frac{(1-\varphi)\rho_f + \varphi\rho_s\left(\frac{\beta_s^*}{\beta_f^*}\right)}{(1-\varphi)\rho_f + \varphi\rho_s}, Q = \frac{\nu^2 Q_0}{k_f u_0^2}, \ Nr = \frac{16\sigma^* T_\infty^3}{3k^* k_f}, \\ Pr_{eff} = \frac{\varphi_3 Pr}{(Nr + \lambda_{nf})}, \\ \lambda_{nf} k_f = k_{nf}, Pr = \frac{(\mu c_p)_f}{k_f}, \lambda^* = \frac{1}{\varphi_3 Pr}, Sc = \frac{\nu}{D}, K_{ch} = \frac{K_1 \nu}{u_0^2}, \\ \varphi_4 = \varphi\frac{(\rho c_p)_s}{(\rho c_p)_f} - (\varphi-1). \end{array} \right\} \qquad (2.17)$$

where the properties of thermophysical *EO* based nanofluid particles are described by the functions $Re, \varphi_1, \varphi_2, \varphi_3$ and φ_4. The parameters $\delta, \xi, Gr, Gm, M, m, Pr, Nr, Q, Sc$ and K_{ch} are respectively Brinkman parameter, rotation parameter, thermal Grashof number, solutal Grashof number, magnetic parameter, Hall parameter, Prandtl number, thermal radiation parameter, heat source parameter, Schmidt number and chemical reaction parameter. Furthermore, Pr_{eff} and $\lambda^* = \frac{1}{\varphi_3 Pr}$ are nanoparticle volume fraction modified Prandtl numbers. The transformed problem is described by Eqs. (2.12)–(2.15) with initial and boundary conditions (2.16). The primary and secondary flow momentum equations (2.12) (2.13) can be further simplified using complex

variable substitutions, and defining a parameter, $\Delta t = \psi t$, where ψ is a constant, to the form:

$$\overline{V}_t = \frac{1}{Re}\overline{V}_{yy} - \lambda_1\overline{V} + Gr^*\overline{\theta} + Gm^*\overline{C} \tag{2.18}$$

where $\overline{V} = \overline{u} + i\overline{w}$, and $\lambda_1 = \frac{M^*(im+1)}{m^2+1} + \delta + i2\xi$ is invariable.

The dimensionless conditions can be modified now to:

$$\left.\begin{array}{l} \overline{V}(y,0) = 0, \overline{\theta}(y,0) = 0, \overline{C}(y,0) = 0, \\ \overline{V}(0,t) = \psi t, \overline{\theta}(0,t) = t, \overline{C}(0,t) = t, \\ \overline{V}(\infty,t) = 0, \overline{\theta}(\infty,t) = 0, \overline{C}(\infty,t) = 0 \end{array}\right\} \tag{2.19}$$

The *homogenized skin friction coefficient, Nusselt number and Sherwood number* are given by

$$\left.\begin{array}{l} 2(1-\varphi)^{2.5}\sqrt{t}C_f = \left(\dfrac{\partial\overline{V}}{\partial\eta}\right)_{\eta=0}, \\[2mm] 2\sqrt{t}Nu = -\left(Nr + \dfrac{k_{nf}}{k_f}\right)\left(\dfrac{\partial\overline{\theta}}{\partial\eta}\right)_{\eta=0}, \\[2mm] Sh = -\left(\dfrac{\partial\overline{C}}{\partial\eta}\right)_{\eta=0}. \end{array}\right\} \tag{2.20}$$

3. Analytical solution procedure

The Eqs. (2.18), (2.14) and (2.15) with conditions (2.19), are solved exactly by the Laplace Transform Method, described in Kreyszig[49] yielding the following results:

3.1. Velocity field

$$Z\left\{\overline{V}_t\right\} = \frac{1}{Re}Z\left\{\overline{V}_{yy} - \lambda_1 Z\left\{\overline{V}\right\} + Gr^*Z\left\{\overline{\theta}\right\} + Gm^*Z\left\{\overline{C}\right\}\right\}, \tag{3.1.1}$$

$$q\overline{\overline{V}} - \overline{V}(y,0) = \frac{1}{Re}\overline{\overline{V}}_{yy}(y,q) - \lambda_1\overline{\overline{V}} + Gr^*\overline{\overline{\theta}} + Gm^*\overline{\overline{C}}, \tag{3.1.2}$$

$$\overline{\overline{V}}_{yy} - Req\overline{\overline{V}} - Re\lambda_1\overline{\overline{V}} + ReGr^*\overline{\overline{\theta}} + ReGm^*\overline{\overline{C}} = 0, \tag{3.1.3}$$

$$\overline{\overline{V}}_{yy} - Re[q+\lambda_1]\overline{\overline{V}} = -Re\left\{Gr^*\overline{\overline{\theta}} + Gm^*\overline{\overline{C}}\right\}, \tag{3.1.4}$$

Which implies:

$$\frac{d^2}{dy^2}\overline{\overline{V}} - Re[q+\lambda_1]\overline{\overline{V}} = -Re\left\{Gr^*\overline{\overline{\theta}} + Gm^*\overline{\overline{C}}\right\} \tag{3.1.5}$$

$$\left.\begin{array}{l} \dfrac{d^2}{dy^2}\overline{\overline{V}} - Re[q+\lambda_1]\overline{\overline{V}} = -ReGr^*\dfrac{1}{q^2}exp\left(-y\sqrt{Pr_{eff}(q-\lambda^2 Q)}\right) \\[3mm] \quad -ReGm^*\dfrac{1}{q^2}exp\left(-y\sqrt{Sc(q-K_{ch})}\right) \end{array}\right\} \tag{3.1.6}$$

The *homogeneous solution* is

$$\left.\begin{array}{l} M^2 - Re[q+\lambda_1] = 0 \Rightarrow m = \pm\sqrt{Re[q+\lambda_1]}, \\[2mm] \overline{\overline{V}}_H = c_1 exp\left(-y\sqrt{Re[q+\lambda_1]}\right) + c_2 exp\left(y\sqrt{Re[q+\lambda_1]}\right) \end{array}\right\} \tag{3.1.7}$$

The *particular solution* is:

$$\overline{\overline{V}}_p = -\frac{ReGr^*}{q}\frac{exp\left(-y\sqrt{Pr_{eff}(q-\lambda^*\varphi)}\right)}{M^2 - Re(q+\lambda_1)}$$

$$\quad - \frac{ReGm^*}{q^2}\frac{exp\left(-y\sqrt{Sc(q-K_{ch})}\right)}{M^2 - Re(q+\lambda_1)}$$

$$\overline{\overline{V}}_p = -\frac{ReGr^*}{q^2}\frac{exp\left(-y\sqrt{Pr_{eff}(q-\lambda^*\varphi)}\right)}{(Pr_{eff})(q-\lambda^*\varphi) - Re(q+\lambda_1)}$$

$$\quad - \frac{ReGm^*}{q^2}\frac{exp\left(-y\sqrt{Sc(q-K_{ch})}\right)}{Sc(q-K_{ch}) - Re(q+\lambda_1)} \tag{3.1.8}$$

Now

$$\overline{\overline{V}} = \overline{\overline{V}}_H + \overline{\overline{V}}_P = c_1\exp\left(-y\sqrt{Re(q+\lambda_1)}\right) + c_2\exp\left(-y\sqrt{Re(q+\lambda_1)}\right)$$

$$\quad - \frac{ReGr^*}{q^2}\frac{exp\left(-y\sqrt{Pr_{eff}(q-\lambda^*\varphi)}\right)}{(Pr_{eff})(q-\lambda^*\varphi) - Re(q+\lambda_1)}$$

$$\quad - \frac{ReGm^*}{q^2}\frac{exp\left(-y\sqrt{Pr_{eff}(q-\lambda^*\varphi)}\right)}{(Sc)(q-K_{Ch}) - Re(q+\lambda_1)} \tag{3.1.9}$$

It follows that:

$$\left.\begin{array}{l} \overline{V}(y,0) = 0 \\ \overline{V}(0,t) = \psi_t \\ \overline{V}(\infty,t) = 0 \end{array}\right\} \Rightarrow \overline{\overline{V}}(y,0) = 0, \overline{\overline{V}}(0,q) = \frac{\psi}{q^2}, \overline{\overline{V}}(\infty,q) = 0.$$

$$\overline{\overline{V}}(0,q) = c_1 + c_2 - \frac{ReGr^*}{q^2\left[Pr_{eff}(q-\lambda^*\varphi) - Re(q+\lambda_1)\right]}$$

$$\quad - \frac{ReGm^*}{q^2\left[Sc(q-K_{ch}) - Re(q+\lambda_1)\right]}$$

$$\frac{\psi}{q^2} = c_1 + c_2 - \frac{ReGr^*}{q^2\left[Pr_{eff}(q-\lambda^*\varphi) - Re(q+\lambda_1)\right]}$$

$$\quad - \frac{ReGm^*}{q^2\left[Sc(q-K_{ch}) - Re(q+\lambda_1)\right]}$$

$$\overline{\overline{V}}(\infty,q) = c_1 \times 0 + c_2 e^\infty - 0 - 0 \Rightarrow 0 = c_2 e^\infty,\ c_2 = 0,\ e^\infty \neq 0,$$

$$c_1 = \frac{\psi}{q^2} + \frac{ReGr^*}{q^2\left[Pr_{eff}(q-\lambda^*\varphi) - Re(q+\lambda_1)\right]}$$

$$\quad + \frac{ReGm^*}{q^2\left[Sc(q-K_{ch}) - Re(q+\lambda_1)\right]}$$

Hence the final form of the velocity solution emerges as:

$$\begin{aligned} \overline{\overline{V}}(y,q) &= \left\{\begin{array}{l}\left[\dfrac{\psi}{q^2} + \dfrac{ReGr^*}{q^2\left[Pr_{eff}(q-\lambda^*\varphi) - Re(q+\lambda_1)\right]}\right.\\[3mm] \left. + \dfrac{ReGm^*}{q^2\left[Sc(q-K_{ch}) - Re(q+\lambda_1)\right]}\right]\\[3mm] exp\left(-y\sqrt{Re(q+\lambda_1)}\right)\end{array}\right\}\\[3mm] &\quad - \frac{ReGr^*}{q^2}\frac{exp\left(-y\sqrt{Pr_{eff}(q-\lambda^*\varphi)}\right)}{Pr_{eff}(q-\lambda^*\varphi) - Re(q+\lambda_1)}\\[3mm] &\quad - -\frac{ReGm^*}{q^2}\frac{exp\left(-y\sqrt{Sc(q-K_{ch})}\right)}{Sc(q-K_{ch}) - Re(q+\lambda_1)} \end{aligned} \tag{3.1.10}$$

3.2. Heat equation

$$Z\left\{\overline{\theta}_t\right\} = \frac{1}{Pr_{eff}}Z\left\{\overline{\theta}_{yy}\right\} + \lambda^*QZ\left\{\overline{\theta}\right\}, \tag{3.2.1}$$

$$Z\left\{f'(t)\right\} = SZ\left\{f(t)\right\} - f(0) \tag{3.2.2}$$

$$SZ\left\{\left(\overline{\theta}(y,t)\right) - \left(\overline{\theta}(y,0)\right)\right\} = \frac{1}{Pr_{eff}}\overline{\theta}_{yy} + \lambda^*Q\overline{\theta}(y,s) \tag{3.2.3}$$

$$S\overline{\overline{\theta}}(y,S) = \frac{1}{Pr_{eff}}\frac{d^2\overline{\overline{\theta}}(y,S)}{dy^2} + \lambda^*Q\overline{\theta}(y,s) \Rightarrow \frac{1}{Pr_{eff}}\frac{d^2\overline{\overline{\theta}}(y,S)}{dy^2}$$

$$\quad + \lambda^*Q\overline{\theta}(y,s) - S\overline{\overline{\theta}}(y,S) = 0 \tag{3.2.4}$$

$$\frac{d^2\overline{\overline{\theta}}(y,S)}{dy^2} + \left(Pr_{eff}\left(\lambda^*Q - S\right)\right)\overline{\overline{\theta}}(y,S) = 0 \tag{3.2.5}$$
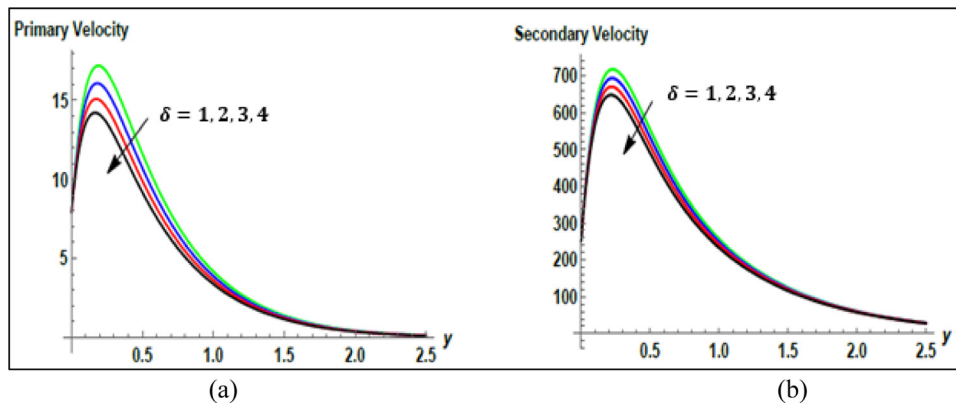
Fig. 2. Variation of (a) Primary velocity (b) secondary velocity profiles for different values of Brinkman parameter, δ.
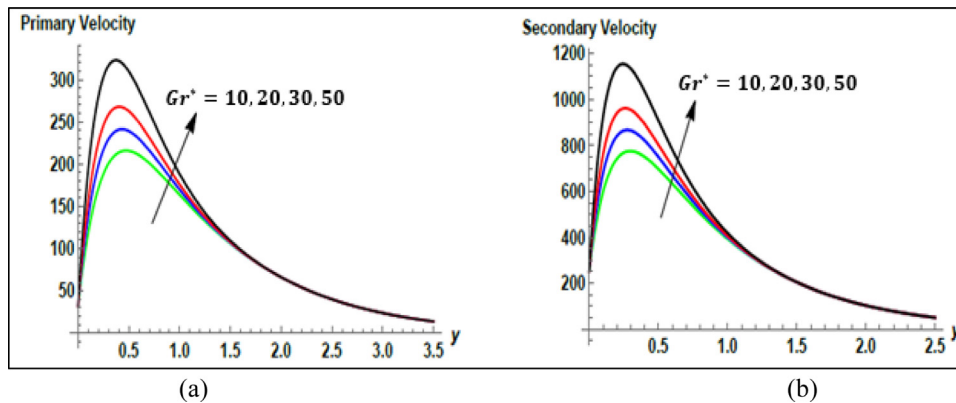

Fig. 3. Variation of (a) Primary velocity (b) secondary velocity profiles for different values of modified thermal Grashof number, Gr^*.

On solving we obtain:

$$\bar{\bar{\theta}}(y,S) = c_1 exp\left(y\sqrt{Pr_{eff}(\lambda^*Q + S)}\right) + c_1 exp\left(-y\sqrt{Pr_{eff}(\lambda^*Q + S)}\right)$$

(3.2.6)

$$\left.\begin{array}{l}\bar{\theta}(0,t) = t \\ \bar{\theta}(\infty,t) = 0\end{array}\right\} \Rightarrow \bar{\bar{\theta}}(0,S) = \frac{1}{S^2}, \bar{\bar{\theta}}(\infty,S) = 0,$$

$$where\ \bar{\bar{\theta}}(y,S) = \frac{1}{S^2}exp\left(-y\sqrt{Pr_{eff}(-\lambda^*Q + S)}\right),$$

$$\frac{1}{S^2} = c_1 + c_2, 0 = c \times \infty, c = 0, \infty \neq 0.$$

3.3. Concentration equation

$$ScZ\left\{\bar{C_t}\right\} = Z\left\{\bar{C}_{yy}\right\} - ScK_{ch}Z\left\{\bar{C}\right\}$$

(3.2.7)

$$\left.\begin{array}{l}qSc\bar{\bar{C}}(y,q) - \bar{C}(y,0) = \bar{\bar{C}}_{yy}(y,q) - ScK_{ch}\bar{\bar{C}}(y,q), \\ \Rightarrow qSc\bar{\bar{C}}(y,q) = \bar{\bar{C}}_{yy}(y,q) - ScK_{ch}\bar{\bar{C}}(y,q)\end{array}\right\}$$

(3.2.8)

Further,

$$0 = \frac{d^2}{dy^2}\bar{\bar{C}}(y,q) - Sc\left[q - K_{ch}\right]\bar{\bar{C}}(y,q)$$

(3.2.9)

On solving the following solution is obtained:

$$\bar{\bar{C}}(y,q) = c_1 exp\left(y\sqrt{Sc(q - K_{ch})}\right) + c_2 exp\left(-y\sqrt{Sc(q - K_{ch})}\right)$$

(3.2.10)

$$\left.\begin{array}{l}\bar{C}(0,t) = t \\ \bar{C}(\infty,t) = 0\end{array}\right\} \Rightarrow Z\left\{\bar{C}(0,t)\right\} = \bar{\bar{C}}(0,q) = \frac{1}{q^2},$$

$$Z\left\{\bar{C}(\infty,t) = \bar{\bar{C}}(\infty,q) = 0,\right\}$$

$$\bar{\bar{C}}(0,q) = c_1 + c_2 \Rightarrow c_1 + c_2 = \frac{1}{q^2},$$

$$\bar{\bar{C}}(\infty,q) = c_1 e^\infty \Rightarrow 0 = c_1 e^\infty, e^\infty \neq 0, c_1 = 0, c_2 = \frac{1}{q^2}$$

$$\bar{\bar{C}}(y,q) = \frac{1}{q^2}exp\left(-y\sqrt{Sc(q - K_{ch})}\right)$$

4. Graphical results and interpretation

Symbolic software has been employed to evaluate the closed form solutions for $\bar{u}, \bar{w}$, thermal field $\bar{\theta}$, solutal field $\bar{C}$ as derived in Section 3. The shear stress C_f, Nusselt number Nu and Sherwood number Sh are computed using the basic solutions, as per the definitions given in Eq. (2.20). The results are displayed in Figs. 2–16. The default values of all parameters are as follows unless stated otherwise: $\phi = 0.1, \xi = 1, m = 0.1, M = 0.1, t = 0.5, Pr = 1000, Nr = 0.5, Gr^* = 0.5, Gm^* = 20, Sc = 0.4, K_{ch} = 0.3, \lambda^* = 0.1, Q = 0.1, \delta = 1$. This data is extracted from Refs. 36, 37, 50, 51 and is representative of actual thermo-solutal nanofluid transport in MHD generators.

Fig. 2 illustrates the evolution in primary and secondary velocity with modification in Brinkman parameter, δ. There is a manifest reduction in both velocity components. The drag force on the nanoparticles is enhanced relative to the inertial force with greater Brinkman parameter. A velocity peak is computed near the wall in both cases; however, the magnitude of the secondary velocity is vastly in excess of the primary velocity. The secondary flow is therefore dominant
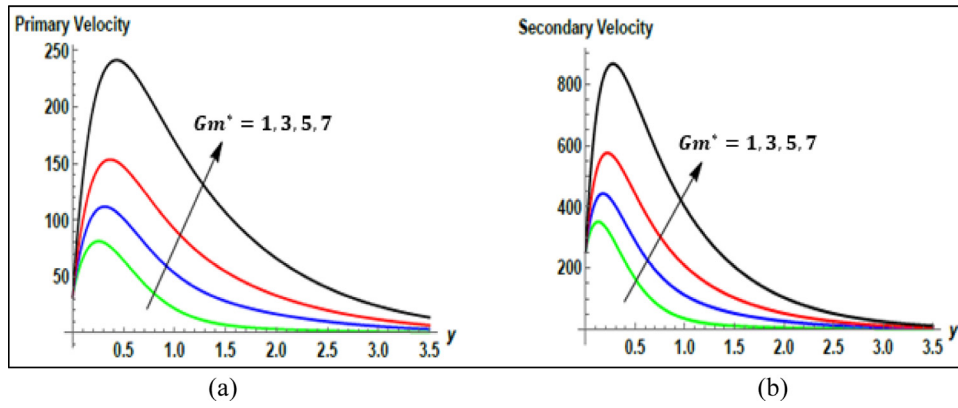
Fig. 4. Variation of (a) Primary velocity (b) secondary velocity profiles for different values of solutal Grashof number, Gm^*.
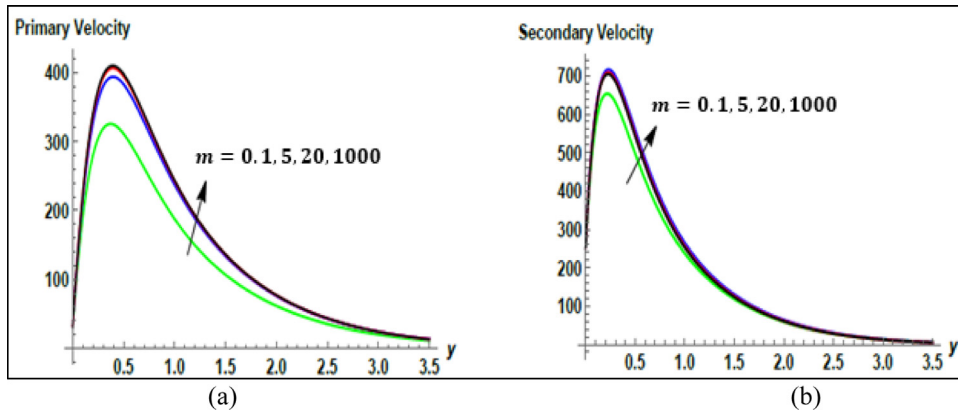

Fig. 5. Variation of (a) Primary velocity (b) secondary velocity profiles for different values of Hall parameter, m.
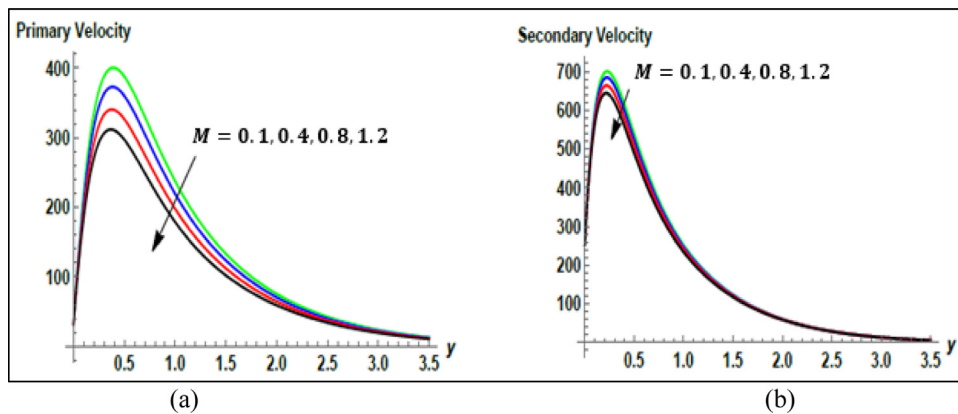

Fig. 6. Variation of (a) Primary velocity (b) secondary velocity profiles for different values of magnetic body force parameter, M.

due to the Hall current effect irrespective of the Brinkman parameter. Asymptotically smooth trends are computed in the free stream (large values of transverse coordinate, y).

Fig. 3 displays the impact of the modified thermal Grashof number on primary and secondary velocity fields. A very strong increment is induced in both components. The conventional thermal Grashof number, $Gr = \frac{(T_w - T_\infty)g\nu\beta_f}{u_0^3}$, is modified via the parameter, $\varphi_2 = \frac{\varphi\rho_s\left(\frac{\beta_s}{\beta_f}\right)-(\varphi-1)\rho_f}{(1-\varphi)\rho_f+\varphi\rho_s}$ as per the Brinkman nanofluid model, to give the modified $Gr^* = Gr\varphi_2$. However, the essential nature of the relative force contributions from thermal buoyancy and viscous resistance remains the same. For $Gr^* = 1$ both these forces contribute equally in the magnetic rotating nanofluid regime. However, for $Gr^* > 1$ (as considered here), significant natural

convection currents are generated in the regime which assists momentum development in both the primary and secondary flows. There is however no significant displacement in the peak near-wall velocity with amplification in modified thermal Grashof number and again the magnitudes of secondary velocity are much greater than primary velocity. Negative values are not present indicating that backflow never arises in the regime.

Fig. 4 shows the distribution of primary and secondary velocity with increment in mass (solutal) Grashof number, Gm^*. Again, this is a factored version of the actual mass Grashof number. $Gm^* = Gm\varphi_3$ where $Gm = \frac{(C_w - C_\infty)g\nu\beta_f^*}{u_0^3}$ and $\varphi_3 = \frac{(1-\varphi)\rho_f+\varphi\rho_s\left(\frac{\beta_s^*}{\beta_f^*}\right)}{(1-\varphi)\rho_f+\varphi\rho_s}$ is a Brinkman

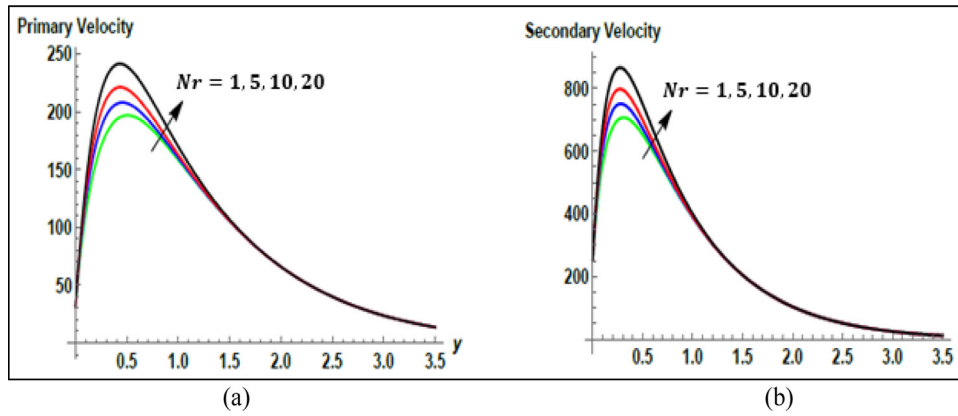**Fig. 7.** Variation of (a) Primary velocity (b) secondary velocity profiles for different values of radiative parameter, Nr.
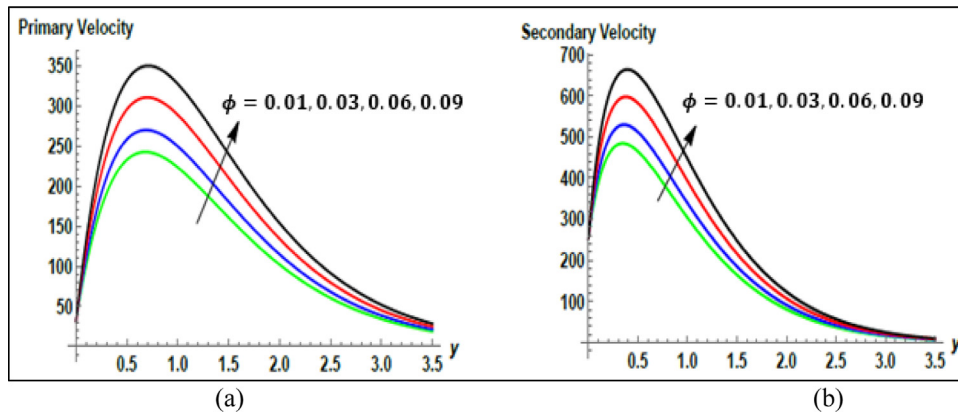

Fig. 8. Variation of (a) Primary velocity (b) secondary velocity profiles for different values of nanoparticle volume fraction, ϕ.
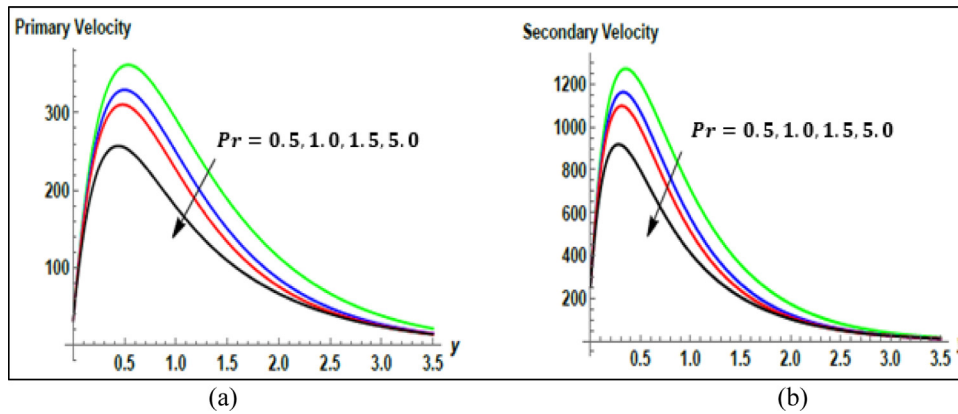

Fig. 9. Variation of (a) Primary velocity (b) secondary velocity profiles for different values of Prandtl number, Pr.

nanoparticle volume fraction coefficient. Strong accentuation in both primary and secondary velocity accompanies a boost in Gm^*. Nanoparticle species buoyancy therefore also accelerates both primary and secondary flow. However, there is in this case a significant shift in the peak velocity for both fields further away from the generator sidewall with increment in solutal Grashof number. The velocity components are therefore strongly enhanced with both thermal and species buoyancy, which will inevitably ramp up the efficiency of the system.

Fig. 5 illustrates the response in primary and secondary velocity to an increment in Hall parameter, m. This key parameter features in both the momentum equations via terms $-\frac{M^*}{1+m^2}\left(\overline{u}+m\overline{w}\right)$ and

$+\frac{M^*}{1+m^2}\left(m\overline{u}-\overline{w}\right)$. The primary and secondary flow are effectively cross-linked via the Hall parameter which also features the magnetic body force term (associated with Lorentzian drag). A more significant enhancement in primary velocity accompanies an increment in Hall parameter, and is sustained for greater distance into the boundary layer, transverse to the generator wall. Although there is an increase in the secondary velocity with Hall parameter, it is weaker and confined to a smaller range near the wall. In both cases, peak velocity near the wall migrates further from the wall with increasing Hall parameter.

Fig. 6 shows the primary and secondary velocity profiles with variation in magnetic body force parameter, M. Larger values of M imply
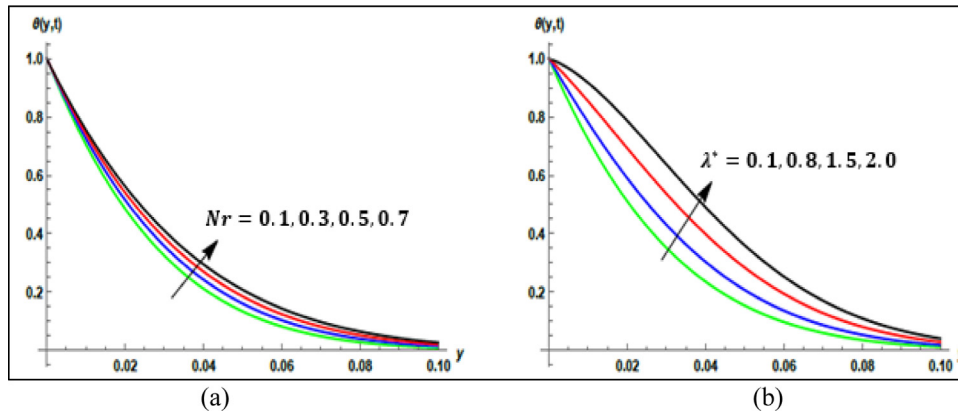
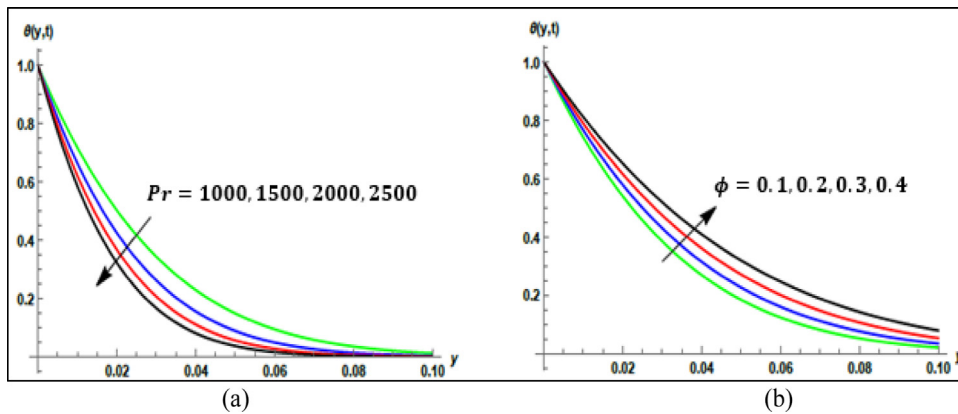**Fig. 10.** Variation of Temperature profiles for different values of (a) Nr (b) λ^*.

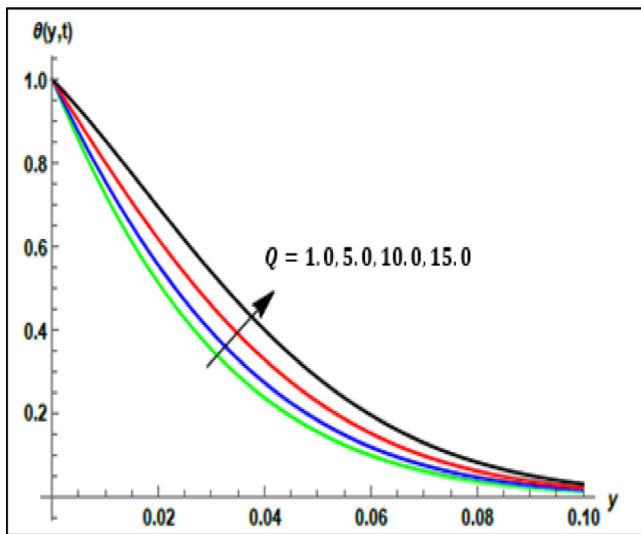**Fig. 11.** Variation of Temperature profiles for different values of (a) Pr (b) ϕ.

Fig. 12. Variation of Temperature profiles for different values of heat source parameter, Q.

a stronger magnetic field influence. The Lorentzian hydromagnetic drag is therefore boosted which decelerates the primary flow strongly and simultaneously pushes the peak velocity further away from the generator wall. Via coupling and the crossflow effect, the secondary velocity is also influenced and damped, but the effect is considerably

weaker than in the primary flow. The overall effect of higher M values is therefore opposite to the Hall parameter influence. Flow deceleration is induced rather than flow acceleration. However, with the judicious combination of these two magnetic effects, the flow structure can be modified for bespoke MHD generator designs and in turn pumping flow rates can be successfully adjusted in the core flow.[51] The boundary layers at the walls are known as Hartmann layers. These will eventually merge together to develop the core flow and have a profound influence on bulk transport in the MHD generator, as will rotation of the duct.

Fig. 7 shows the response in primary and secondary velocity to a change in radiative parameter, Nr. This parameter arises in the transformed heat equation, (14) and augments thermal diffusion. Increasing radiative flux is generated with larger values of Nr which energizes the boundary layer and boosts temperatures. Thermal boundary layer thickness will therefore also be increased. This will aid momentum development and accelerate the primary and secondary flow. The effect is most prominent near the generator wall, in the vicinity of the application of the flux but is progressively diminished further from the wall.

Fig. 8 plots the primary and secondary velocity through the boundary layer transverse to the wall with variation in nanoparticle volume fraction, ϕ. Many terms in the momentum Eq. (12) are influenced by volume fraction coefficients, e.g. $+Gr^*\bar{\theta}, Gm^*\overline{C}, -\frac{M^*}{1+m^2}(\bar{u}+m\bar{w})$ etc. The heat Eq. (14) is also influenced via the terms, $\frac{1}{Pr_{eff}}\theta_{yy}, \lambda^*Q\bar{\theta}$ where

$Pr_{eff} = \frac{\varphi_3 Pr}{(Nr+\lambda_{nf})}, \lambda^* = \frac{1}{\varphi_3 Pr}$ and $\varphi_3 = \frac{(1-\varphi)\rho_f + \varphi\rho_s\left(\frac{\beta_s^*}{\beta_f^*}\right)}{(1-\varphi)\rho_f + \varphi\rho_s}$ (one of several Brinkman coefficients). The dominant influence of increasing volume fraction is to enhance both temperatures and indirectly the
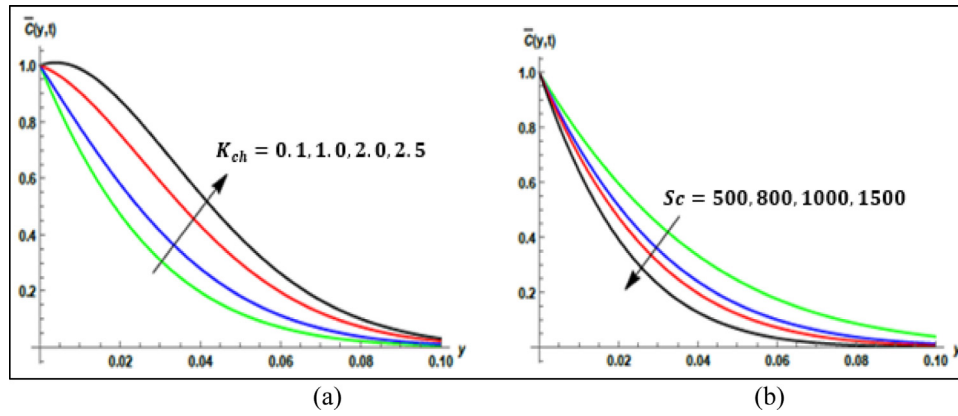
Fig. 13. Variation of concentration profiles for different values of (a) chemical reaction parameter, K_{ch} (b) Schmidt number, Sc.
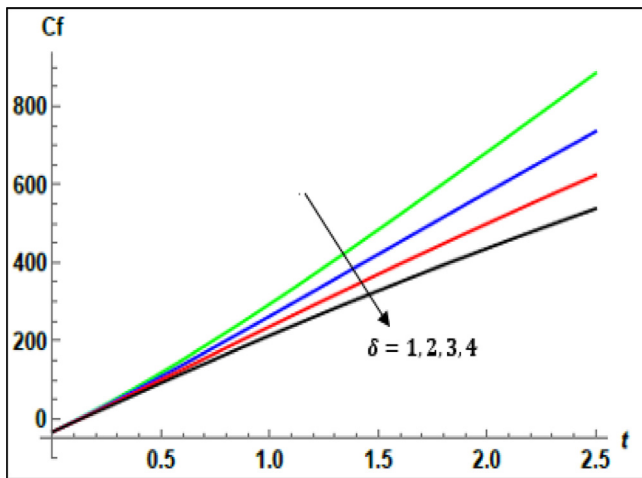

Fig. 14. Variation of skin friction against Brinkman parameter, δ.

primary and secondary flow via viscosity modification in the nanofluid. Over a doping range of 1 to 9% ($\phi = 0.01$ to 0.09) increasing presence of Molybdenum disulphide nanoparticles therefore accelerates the primary and secondary flow. In both cases there is also a slight translocation in the peak velocity further from the generator wall. Again, much higher magnitudes are computed for the secondary flow.

Fig. 9 visualizes the influence of Prandtl number on primary and secondary velocity profiles. A significant decrement is induced in both flow fields with increasing Prandtl number. Pr is inversely proportional to thermal conductivity. As thermal conductivity of the magnetized nanofluid is reduced the Prandtl number is increased. The suppression in thermal conduction in the nanofluid influences the momentum transfer also due to the coupling nature of the thermal buoyancy effect (natural convection). This retards the flow and reduces both primary and secondary flow. Prandtl number also embodies the ratio of momentum diffusion to thermal diffusion in the regime. When Prandtl number equals unity both momentum and heat diffuse at the same rates. For $Pr < 1$ thermal diffusion dominates. For $Pr > 1$ thermal diffusion is dominated. Clearly the thermal diffusivity of the magnetic nanofluid is critical also in manipulating flow characteristics in the rotating wall boundary layer regime. The peak primary and secondary velocity is displaced closer to the wall with increment in Prandtl number. A greater percentage change in primary velocity is computed over the same increment in Prandtl number, although secondary velocity magnitudes are again considerably higher due to the Hall current effect.

Figs. 10–12 illustrate the temperature distributions and reactive species concentration in the boundary layer with variation in selected parameters. In Fig. 10a, an increment in radiative parameter, Nr, considerably *elevates* temperatures. This pattern is sustained through the boundary layer transverse to the generator wall i.e. at all y-values. A strong enhancement in thermal diffusion is induced by the energizing effect of the radiative flux. However, a temperature overshoot is not observed near the wall. The radiative flux exerts a homogeneous effect on the temperature evolution, which is characteristic of the Rosseland diffusion flux model. This also thickens the thermal boundary layer. Radiative equilibrium is achieved, and radiation acts purely diffusively with source terms due to emission. However, this model is restricted to gray fluent media and very high optical thicknesses. Nevertheless, it is evident that temperature augmentation is captured which is not possible when radiative effects are ignored in the mathematical model. In turn this will influence the thermal efficiency of the MHD generator. For more complex simulations recourse to a more elaborate radiative model would be required such as the Chandrasekhar discrete ordinates model (DOM) which can also accommodate specular radiation and transmittivity and reflectivity of the MHD generator wall. Efforts in this direction are underway. Fig. 10b shows that with modified inverse Prandtl number parameter, $\lambda^* = \frac{1}{\varphi_3 Pr}$, there is again an accentuation in temperature magnitudes through the boundary layer. The topology of the temperature profiles is also morphed at very high value of λ^* (=2.0). The presence of the parameter $\varphi_3 = \frac{(1-\varphi)\rho_f + \varphi\rho_s\left(\frac{\beta_s^*}{\beta_f^*}\right)}{(1-\varphi)\rho_f + \varphi\rho_s}$ also indicates that volume fraction of the MoS$_2$ nanoparticles (and other thermal parameters) strongly contributes to the modification in temperatures. Micro-convection around the nanoparticles is intensified with greater percentage doping in the base fluid. This globally affects thermal diffusion in the regime and creates a strong heating effect. It is noteworthy however that an upper limit exists to the nanoparticle volume fraction for which a beneficial effect is achieved. Excessive volume fractions can lead to clustering of nanoparticles and inhibition of thermal diffusion, as noted by Zhou et al.[27] and Reddy et al.[30] MHD generator designers can therefore exploit the doping of the conducting fluid with magnetic nanoparticles up to a certain threshold beyond which counter-productive effects are witnessed. This area clearly requires further investigation, and it is hoped that the present theoretical analysis will motivate experimental studies to better elaborate the performance of MoS$_2$ nanoparticles in rotating generators. Fig. 11a shows that at very high Prandtl numbers (representative of liquid-metal based pumping fluids), again temperatures are very strongly suppressed in the regime. The massive thermal conductivities of such liquids inevitably contribute to significant reduction in thermal diffusion and are usually deployed for controlling excessive temperatures as noted by Rosa.[51] With increasing nanoparticle volume fractions, Fig. 11b demonstrates that considerable thermal enhancement is produced in the regime. Temperatures are very strongly boosted at all locations from the generator wall. Thermal boundary layer thickness is also elevated. Fig. 12
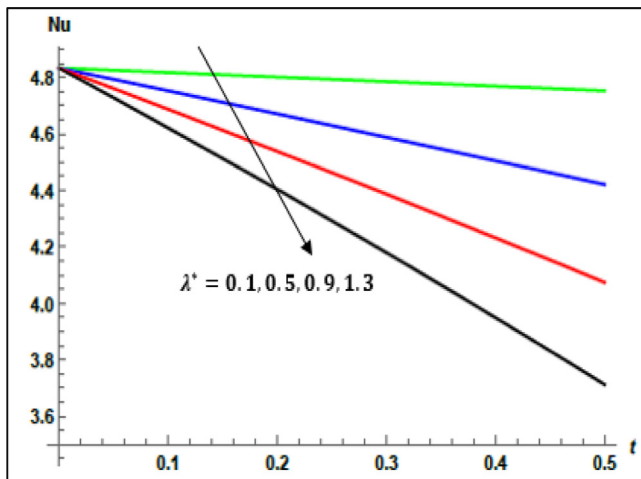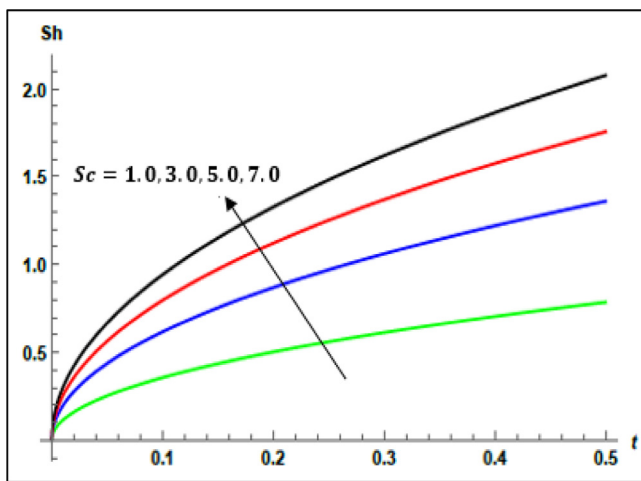
Fig. 15. Variation of Nusselt number against λ^*.

Fig. 16. Variation of Sherwood number against Schmidt number, Sc.

shows that an increase in heat source parameter, Q, as anticipated, also significantly enhances temperatures. Volumetric heat generation in the MoS$_2$-oil working nanofluid is boosted with heat source effect. Thermal boundary layer thickness will also experience and upsurge. Fig. 13a reveals that with increasing constructive chemical reaction rate, K_{ch}, there is a hike in concentration magnitudes. This effect may be useful for simulating corrosion behavior in the vicinity of the generator wall. As K_{ch} increases, the intensification of chemical reaction produces more of the original species. This boosts concentration magnitudes and increases the concentration (species) boundary layer thickness. A concentration overshoot is also computed at maximum value of K_{ch} which is absent at lower values (weaker chemical reaction). Koester and Perkins[43] have noted that reactivity of the species diffusing which may be oxygen or another gas, requires careful control, to mitigate the *so-called slagging or high deposition clustering effect* encountered in MHD generators at the electrodes as this can adversely affect the generator performance and lead to operational downtimes for cleaning to be administered. Fig. 13b shows that with greater Schmidt number, however, the reverse effect to chemical reaction is induced. Concentration magnitudes are suppressed strongly. The lower molecular diffusivity of the reactive species contributes to the plummet in species diffusion. This depletes molecular diffusion of the species and also reduces species boundary layer thickness at the MHD generator wall.

Figs. 14–16 display the impact of selected parameters on skin friction, Nusselt number and Sherwood number. Increasing Brinkman parameter, δ, as observed in Fig. 14, logically reduces the skin friction since the drag effect on the nanoparticles is increased. There is however a strong boost in skin friction with time (t) irrespective of the Brinkman parameter effect. Flow acceleration is therefore achieved with elapse in time, which will result in enhanced pumping flow rates in the generator. Fig. 15 shows a decrement is induced in Nusselt number with increasing modified inverse Prandtl number parameter, $\lambda^* = \frac{1}{\varphi_3 Pr}$. The profiles also transition from approximate linear decay at low values of this parameter to parabolic decays at higher values. The quantity of heat transferred to the generator wall is suppressed since as noted in Fig. 10b, temperatures within the boundary layer are increased. A strong cooling effect is therefore achieved at the wall which is advantageous for operations. With progression in time, Nusselt number is also depleted strongly. The relative contribution of thermal convection to thermal conduction at the wall is therefore also diminished. Again, this is critical from the viewpoint of temperature control at the boundaries since the primary objective in MHD generators is high core thermal efficiencies (away from the wall) as emphasized by Rosa.[51] Although we have not studied explicitly the effect of rotation of the duct on the wall heat transfer characteristics, it will also contribute markedly, and a careful balance has to be maintained between all parameters to achieve desired and sustainable thermal efficiency for robust energy production. Finally, Fig. 16 shows the evolution in Sherwood number with increasing Schmidt number (Sc) and time (t). The mass transfer of reactive species from the bulk flow within the boundary layer to the generator wall is enhanced with higher Schmidt numbers. The decrease in molecular diffusivity implies that less reactive species is transferred from the wall to the interior of the boundary layer. Therefore, greater molecular diffusion from the boundary layer to the generator wall is produced. This must of course be controlled to avoid as described earlier, excessive deposition of species on the boundary which can exacerbate corrosion effects on the electrodes. With greater time elapse, a substantial elevation in Sherwood number is computed, as shown by the monotonic growths. Mass transfer of the reactive species to the generator wall is therefore elevated.

5. Conclusions

Inspired by probing emerging designs in nanofluid-based rotating Hall MHD generator systems, a theoretical study of the combined effects of Hall current, heat source, chemical reaction and radiative flux on the unsteady rotating thermo-solutal magnetohydrodynamic boundary layer transport of Molybdenum disulphide (MoS$_2$)-EO oil electroconductive nanofluid on the side wall is presented. Chemical reaction effects have been included due to corrosion characteristics encountered in real MHD generators at the electrode walls. Thermal and species buoyancy effects have also been included in the model. The generalized Brinkman nanofluid formulation has been adopted. The governing dimensional conservation equations are rendered non-dimensional via suitable transformations and the emerging system of dimensionless coupled partial differential equations with associated initial and boundary conditions, is solved analytically with the Laplace Transform Method (LTM) and complex variables. A detailed parametric study of the influence of key control parameters on primary and secondary (cross flow) velocity, temperature and concentration, skin friction, Nusselt number and Sherwood number has been conducted. The simulations have shown:

- Primary and secondary velocity are reduced with increment in Brinkman parameter (ratio of drag force on nanoparticle to inertial force) and magnetic body force parameter.
- Primary and secondary velocity are elevated with increasing modified thermal Grashof number, solutal Grashof number, Hall parameter, nanoparticle volume fraction and Rosseland radiative flux parameter.

- Temperature and thermal boundary layer thickness are suppressed with increasing Prandtl number but elevated with increasing radiative parameter, nanoparticle volume fraction and heat source parameter.
- Concentration experiences a strong decrement with greater Schmidt number whereas it is elevated with chemical reaction rate parameter (constructive chemical reaction).
- Skin friction is decreased with greater Brinkman parameter due to the greater drag force dominance on nanoparticles whereas it is increased with time.
- Nusselt number is depleted with greater inverse Brinkman volume fraction parameter and also reduced with progression in time.
- Sherwood number is enhanced with Schmidt number (i.e. with lower molecular diffusivity) but strongly accentuated with increasing time.

The present simulations have revealed some interesting insights into rotating MHD generator near-wall boundary layer characteristics for magnetic nanofluids. However, the analysis has ignored magnetic induction and Maxwell displacement current effects[52] which also play an important role in operations. These aspects may be considered in future studies. Additionally, a more complex radiative transfer model e.g. Chandrasekhar discrete ordinates model or the P1 differential approximation[53] may also be considered to better represent spectral characteristics and a range of optical thicknesses for the working fluid. Efforts in these directions are underway and will be communicated imminently.

Declaration of competing interest

The authors declare that they have no known competing financial interests or personal relationships that could have appeared to influence the work reported in this paper.

Data availability

No data was used for the research described in the article

References

1. Jiménez-Flores S, Pérez-Luna G, Alvarado-Pulido JJ, Jiménez-Gonzalez AE. Development and simulation of a magnetohydrodynamic solar generator operated with NaCl electrolyte solution. *J Sol Energy Eng*. 2021;143(2):021004. http://dx.doi.org/10.1115/1.4048013.
2. Ibáñez G. Optimization analysis of an alternate magnetohydrodynamic generator. *Energy Conv Managm*. 2002;43:1757–1771.
3. Hardianto T. Three-dimensional flow analysis in a Faraday-type MHD generator. *IEEE Tranac Ind Appl*. 2008;44:1116–1123.
4. Siva Reddy S, Anwar Bég O, Modugula P, Kadir A. Computation of transient radiative reactive thermo-solutal magneto-hydrodynamic convection in inclined MHD hall generator flow with dissipation and cross diffusion. *Comput Therm Sci*. 2019;11(6):541–563.
5. Intani P, Sasaki T, Kikuchi T, Harada N. Analysis of disk AC MHD generator performance by finite element method. *J Plasma Fusion Res Ser*. 2010;9:580–585.
6. Heywood JB, Womack GJ. *Open-Cycle MHD Power Generation*. New York, NY: Pergamon Press; 1969.
7. Sutton GW, Sherman AS. *Engineering Magnetohydrodynamics*. New York, NY: McGraw-Hill; 1965.
8. Liberati A, Okuno Y. Influence of anode-region boundary-layer separation on disk MHD-generator performance. *IEEE Transac Plasma Sci*. 2007;35:1588–1597.
9. Anwar Bég O, Ferdows M, Enamul Karim M, et al. Computation of non-isothermal thermo-convective micropolar fluid dynamics in a Hall MHD generator system with non-linear distending wall. *Int J Appl Comput Math*. 2020;6:42. http://dx.doi.org/10.1007/s40819-020-0792.
10. Pengyu Y, Zhang B, Li Y, et al. Investigation of MHD power generation with supersonic non-equilibrium RF discharge. *Chin J Aeronautics*. 2016;29:855–862.
11. Biswas D, Matsubara H, Kabashima S, Yamasaki H, Shioda S. Boundary layer effects in He and Ar driven disk MHD generators. *Energy Conv Managm*. 1988;28:105–115.
12. Hussain SM, Jain J, Seth GS, Rashidi MM. Free convective heat transfer with Hall effects, heat absorption and chemical reaction over an accelerated moving plate in a rotating system. *J Magn Magn Mater*. 2017;422:112–123.
13. Seth GS, Sarkar S, Hussain SM, Mahato GK. Effects of hall current and rotation on hydromagnetic natural convection flow with heat and mass transfer of a heat-absorbing fluid past an impulsively moving vertical plate with ramped temperature. *J Appl Fluid Mech*. 2015;8(1):159–171.
14. Anwar Bég O, Sim L, Zueco J, Bhargava R. Numerical study of magnetohydrodynamic viscous plasma flow in rotating porous media with hall currents and inclined magnetic field influence. *Commun Nonlinear Sci Numer Simul*. 2010;15:345–359.
15. Choi SUS. Enhancing thermal conductivity of fluids with nanoparticles. In: Siginer DA, Wang HP, eds. *Developments and Applications of Non-Newtonian Flows*. New York, NY: American Society of Mechanical Engineers; 1995.
16. Choi C, Yoo HS, Oh JM. Preparation and heat transfer properties of nanoparticle-in-transformer oil dispersions as advanced energy-efficient coolants. *Curr Appl Phys*. 2008;8(6):710–712.
17. Duan M, Shapter JG, Qi W, Yang S, Gao G. Recent progress in magnetic nanoparticles: Synthesis, properties, and applications. *Nanotech*. 2018;29(45):452001. http://dx.doi.org/10.1088/1361-6528/aadcec.
18. Hosono T, Takahashi H, Fujit A, Justin JR, Tohji K, Jayadevan B. Synthesis of magnetite nanoparticles for AC magnetic heating. *J Magn Magn Mater*. 2009;321(19):3019–3023.
19. Thirumurugan A, Prabhakaran K, Uday Bhaskar R, Mangalaraja RV, Akbari-Fakhrabadi A. Carbon decorated octahedral shaped Fe_3O_4 and α-Fe_2O_3 magnetic hybrid nanomaterials for next generation supercapacitor applications. *Appl Surf Sci*. 2019;485:147–157.
20. Ramadoss A, Kim SJ. Improved activity of a graphene–TiO_2 hybrid electrode in an electrochemical supercapacitor. *Carbon*. 2013;63:434–445.
21. Balakin BV, Stava M, Kosinka A. Photothermal convection of a magnetic nanofluid in a direct absorption solar collector. *Sol Energy*. 2022;239:33–39.
22. Wang D, Wang L, Zhu G, et al. Magnetic photothermal nanofluids with excellent reusability for direct absorption solar collectors. *ACS Appl Energy Mater*. 2018;1(8):3860–3868.
23. Liu J, Martin PF, McGrail BP. Rare-earth element extraction from geothermal brine using magnetic core–shell nanoparticles-techno-economic analysis. *Geothermics*. 2021;89:101938. http://dx.doi.org/10.1016/j.geothermics.2020.101938.
24. Jung YS, Choi HJ, Park SH, Kim D, Park SH, Cho YS. Nanoampere-level piezoelectric energy harvesting performance of lithography-free centimetre-scale MoS_2 monolayer film generators. *Small*. 2022;18(24):2200184. http://dx.doi.org/10.1002/smll.202200184.
25. Wang X, Shi W, Wan J. Enhanced piezoelectric effect in MoS_2 and surface engineered GaN bilayer. *J Appl Phys*. 2021;130(1):015113. http://dx.doi.org/10.1063/5.0055321.
26. Shirokura T, Muneta I, Kakushima K, Tsutsui K, Wakabayashi H. Strong edge-induced ferromagnetism in sputtered MoS_2 film treated by post-annealing. *Appl Phys Lett*. 2019;115(19):192404. http://dx.doi.org/10.1063/1.5118913.
27. Zhou Q, Su S, Cheng P, et al. Robust ferromagnetism in zigzag-edge rich MoS_2 pyramids. *Nanoscale*. 2018;10(24):11578–11584. http://dx.doi.org/10.1039/C8NR03038C.
28. Chamkha AJ, Issa C, Khanafer K. Natural convection from an inclined plate embedded in a variable porosity porous medium due to solar radiation. *Int J Therm Sci*. 2002;41(1):73–81.
29. Wakif A, Chamkha AJ, Animasaun IL, Zaydan M, Waqas H, Sehaqui R. Novel physical insights into the thermodynamic irreversibilities within dissipative EMHD fluid flows past over a moving horizontal riga plate in the coexistence of wall suction and joule heating effects: A comprehensive numerical investigation. *Arab J Sci Eng*. 2020;45:9423–9438.
30. Reddy PR, Gaffar SA, Anwar Bég O, Khan BMH. Hall and ion slip effects on nanofluid transport from a vertical surface: Buongiorno's model. *Z Angew Math Mech*. 2022;102(3):e202000174. http://dx.doi.org/10.1002/zamm.202000174.
31. Wahid MA, Akl M. Effect of hall current on MHD flow of a nanofluid with variable properties due to a rotating disk with viscous dissipation and nonlinear thermal radiation. *AIP Adv*. 2016;6:095308. http://dx.doi.org/10.1063/1.4962961.
32. Gumber P, Yaseen M, Rawat SK, Kumar M. Heat transfer in micropolar hybrid nanofluid flow past a vertical plate in the presence of thermal radiation and suction/injection effects. *Partial Differ Equ Appl Math*. 2022;5:100240. http://dx.doi.org/10.1016/j.padiff.2021.100240.
33. Ali K, Reddy YR, Shekar BC. Thermo-fluidic transport process in magnetohydrodynamic couette channel containing hybrid nanofluid. *Partial Differ Equ Appl Math*. 2023;7:100468. http://dx.doi.org/10.1016/j.padiff.2022.100468.
34. Takhar HS, Chamkha AJ, Nath G. MHD flow over a moving plate in a rotating fluid with magnetic field, Hall Currents and Free Stream Velocity. *Int J Eng Sci*. 2002;40(13):1511–1527.
35. Khan I. Shape effects of MoS_2 nanoparticles on MHD slip flow of molybdenum disulphide nanofluid in a porous medium. *J Mol Liq*. 2017;233:442–451.
36. Jan SAA, Ali F, Sheikh NA, Khan I, Saqib M, Gohar M. Engine oil-based generalized brinkman-type nano-liquid with molybdenum disulfide nanoparticles of spherical shape, Atangana-Baleanu fractional model. *Numer Methods Partial Diff Equ*. 2017;34(5):1472–1488.

37. Ali F, Aamina B, Khan I, Sheikh NA, Saqib M. The magnetohydrodynamic flow of Brinkman-type engine oil based MoS$_2$-nanofuid in a rotating disk with Hall effect. *Int J Heat Technol*. 2017;4:893–902.

38. Mishra A, Upreti H. A comparative study of Ag-MgO/water and Fe$_3$O$_4$-CoFe$_2$O$_4$/EG -water hybrid nanofluid flow over a curved surface with chemical reaction using Buongiorno model. *Partial Differ Equ Appl Math*. 2022;5:100322. http://dx.doi.org/10.1016/j.padiff.2022.100322.

39. Afridi MI, Qasim M, Salman S. Second law analysis of three-dimensional dissipative flow of hybrid nanofluid. *J Nanofluids*. 2018;7(6):1272–1280.

40. Afridi MI, Qasim M, Khan NA, Hamdani M. Heat transfer analysis of Cu-Al$_2$O$_3$-water and Cu-Al$_2$O$_3$-kerosene oil hybrid nanofluids in the presence of frictional heating: Using 3-stage Lobatto IIIA formula. *J Nanofluids*. 2019;8(4):885–891.

41. Afridi MI, Alkanhal TA, Qasim M, Tlili I. Entropy generation in Cu-Al$_2$O$_3$ − H$_2$O hybrid nanofluid flow over a curved surface with thermal dissipation. *Entropy*. 2019;21(10):941. http://dx.doi.org/10.3390/en21100941.

42. Afridi MI, Tlili I, Goodarzi M, Osman M, Khan NA. Irreversibility analysis of hybrid nanofluid flow over a thin needle with effects of energy dissipation. *Symmetry*. 2019;11(5):663. http://dx.doi.org/10.3390/sym11050663.

43. Koester JK, Perkins RA. Discharge and corrosion characteristics of slagging metal electrodes for MHD power generators. *J Mater Energy Syst*. 1979;1:41–54.

44. Kadir A, Anwar Beg O, El Gendy M, Beg TA, Shamshuddin MD. Computational fluid dynamic and thermal stress analysis of coating for high temperature corrosion protection of aerospace gas turbine blades. *Heat Transf Asian Res*. 2019;48:2302–2328.

45. Krishna MV, Chamkha AJ. Hall and ion slip effects on MHD rotating boundary layer flow of nanofluid past an infinite vertical plate embedded in a porous medium. *Results Phys*. 2019;15:102652. http://dx.doi.org/10.1016/j.rinp.2019.102652.

46. Krishna MV, Ahamad NA, Chamkha AJ. Hall and ion slip effects on unsteady MHD free convective rotating flow through a saturated porous medium over an exponential accelerated plate. *Alex Eng J*. 2020;59(2):565–577.

47. Cramer KC, Pai SI. *Magnetofluid Dynamics for Engineers and Applied Physicists*. New York NY: McGraw-Hill; 1973.

48. Oztop HF, Nada EA. Numerical study of natural convection in partially heated rectangular enclosures filled with nanofluids. *Int J Heat Fluid Flow*. 2008;29(5):1326–1336.

49. Kreyszig E. *Advanced Engineering Mathematics*. 10th ed. New York, NY: Wiley; 2010.

50. Sattler KD ed, *Handbook of Nanophysics: Nanoparticles and Quantum Dots*. London: Routledge; 2010.

51. Rosa RJ. *Magnetohydrodynamic Energy Conversion*. Washington, DC: Hemisphere Pub Corp; 1987.

52. Anwar Bég O, Bég TA, Munjam SR, Jangili S. Homotopy and adomain semi-numerical solutions for oscillatory flow of partially ionized dielectric hydrogen gas in a rotating MHD energy generator duct. *Int J Hydrogen Energy*. 2021;46:17677–17696.

53. Zaporowski B, Roszkiewicz J. Radiation heat transfer in the MHD generator. In: Carvalho MG, Lockwood MC, Taine J, eds. *Heat Transfer in Radiating and Combusting Systems*. Berlin, Heidelberg: Springer-Verlag; 1991:491–507.